

Integration of Electrochemical Microsupercapacitors with Thin Film Electronics for On-Chip Energy Storage

Mrinal K. Hota, Qiu Jiang, Zhenwei Wang, Zhong Lin Wang, Khaled N. Salama,* and Husam N. Alshareef*

The development of self-powered electronic systems requires integration of on-chip energy-storage units to interface with various types of energy harvesters, which are intermittent by nature. Most studies have involved on-chip electrochemical microsupercapacitors that have been interfaced with energy harvesters through bulky Si-based rectifiers that are difficult to integrate. This study demonstrates transistor-level integration of electrochemical microsupercapacitors and thin film transistor rectifiers. In this approach, the thin film transistors, thin film rectifiers, and electrochemical microsupercapacitors share the same electrode material for all, which allows for a highly integrated electrochemical on-chip storage solution. The thin film rectifiers are shown to be capable of rectifying AC signal input from either triboelectric nanogenerators or standard function generators. In addition, electrochemical microsupercapacitors exhibit exceptionally slow self-discharge rate ($\approx 18.75 \text{ mV h}^{-1}$) and sufficient power to drive various electronic devices. This study opens a new avenue for developing compact on-chip electrochemical micropower units integrated with thin film electronics.

technologies such as piezoelectric, triboelectric, thermoelectric micropower generators. These energy harvesting approaches are all intermittent by nature. Hence, self-powered devices require the integration of on-chip energy-storage unit to work in tandem with the energy harvester.^[5,6] However, conventional batteries lack the necessary cycle life and cannot deliver the required high power for applications where battery replacement may not be practical (e.g., implantable medical biosensors, remote sensors, sensors for structural health monitoring, and IoT sensors). In contrast, microsupercapacitors (MSCs) have very long cycle life, fast charging rates, and high-power density.^[7–12] In addition, by drawing the maximum current that the source can supply, MSCs charge more efficiently compared to thin film batteries, making supercapacitors more suitable for self-

In recent years, autonomous and self-powered electronic devices started playing an increasingly important role especially in applications such as wearable electronic devices, epidermal electronic sensors, and sensors for the internet of things (IoT).^[1–4] This gave rise to a range of energy harvesting

powered system applications in which the harvester-generated voltage may be variable.^[13]


In order to store energy from such intermittent harvesters, the AC signal must first be rectified before being stored in an electrochemical capacitor. Many publications on self-powered devices use off-the-shelf bulky rectifiers at the interface between the nanogenerator AC signal and a storage capacitor.^[14,15] These rectifiers, which are made using conventional silicon-based p–n or Schottky junction diodes, are bulky as they are packaged inside IC chip carriers, which makes miniaturization of the nanogenerator–electrochemical supercapacitor system challenging. It is therefore important to replace these bulky rectifiers with rectifiers fabricated using thin film electronics technology integrated on the same chip with electrochemical capacitors.

In this work, we propose a new approach to integrate electrochemical microsupercapacitors on-chip with thin film transistors (TFTs) and rectifiers to fabricate a highly integrated monolith rectifier–storage unit. A unique aspect of this work is that we use the same material for both transistor gate electrodes and microsupercapacitors electrodes, which significantly simplifies the fabrication process leading to easy integration with nanogenerator and sensor. The integrated microsupercapacitors–thin film rectifier system performance is demonstrated using signals generated from triboelectric nanogenerators as well as function generators. The performances of the microsupercapacitors,

Dr. M. K. Hota, Dr. Q. Jiang, Dr. Z. Wang, Prof. H. N. Alshareef
Materials Science and Engineering
Physical Science and Engineering Division
King Abdullah University of Science and Technology (KAUST)
Thuwal 23955–6900, Saudi Arabia
E-mail: husam.alshareef@kaust.edu.sa

Prof. Z. L. Wang
School of Materials Science and Engineering
Georgia Institute of Technology
Atlanta, GA 30332-0245, USA

Prof. K. N. Salama
Sensors lab
Advanced Membranes, and Porous Materials Center
Computer, Electrical, and Mathematical Science
and Engineering Division
King Abdullah University of Science and Technology (KAUST)
Thuwal 23955–6900, Saudi Arabia
E-mail: khaled.salama@kaust.edu.sa

 The ORCID identification number(s) for the author(s) of this article can be found under <https://doi.org/10.1002/adma.201807450>.

DOI: 10.1002/adma.201807450

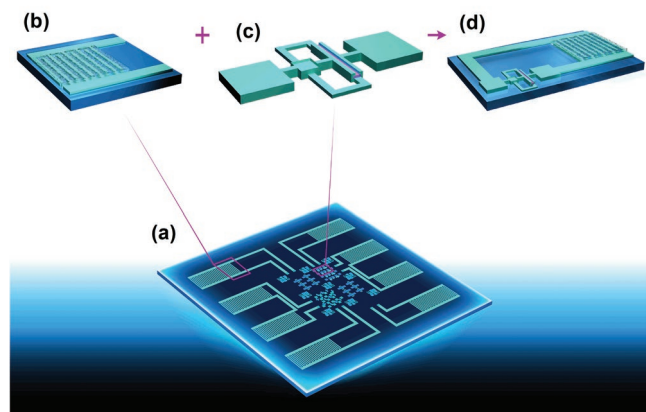


Figure 1. a) Schematic illustration of the integrated microsupercapacitors-thin film rectifier circuits fabricated on a glass substrate. b) The microsupercapacitors, c) the field-effect rectifier, and d) a typical single microsupercapacitors/rectifier unit. In some cases, multiple microsupercapacitors were connected to increase the output potential.

thin film transistor rectifiers, and integrated system show that it is a promising approach for self-power system applications.

Figure 1a shows a schematic illustration of our device concept. The unit consists of microsupercapacitors (Figure 1b) fabricated using a total of 30 fingers of length 2350 μm each that have 100 μm width each and 50 μm spacings between

them having a total surface area of 0.096 cm^2 . The rectifier circuits (Figure 1c) were fabricated on the same substrate. By using RuO_2 as a common electrode material for both the microsupercapacitors and transistor electrodes, a compact rectifier–electrochemical microsupercapacitors device was fabricated as shown in Figure 1d. The schematic of the device process flow is illustrated in Figure S1a (see Supporting Information Section).

RuO_2 was selected as electrode material for both thin film transistors and electrochemical microsupercapacitors for several reasons: 1) it is a well-known pseudocapacitive electrode material, 2) it exhibits metallic conductivity, which is an important characteristic for microsupercapacitors and transistor electrode materials, 3) it has good cycling stability, and 4) our RuO_2 process shows very good self-discharge characteristics, when processed with the appropriate microstructure, as we show later.

Different RuO_2 thin films were prepared on glass substrates at room temperature by reactive magnetron sputtering in a gas mixture of Ar and O_2 using a ruthenium metal target. The electrical resistivity of different RuO_2 thin films was studied using four-probe measurements as a function of oxygen partial pressure (O_{pp}) and RF power. It was found that the resistivity increases with increasing O_{pp} (Figure 2a) but decreases with increasing deposition RF power (Figure S2a, Supporting Information). Film crystallinity was found to improve with RF power, leading to a more ordered film and hence resistivity decreases.^[16] It should be noted, however, that the resistivity

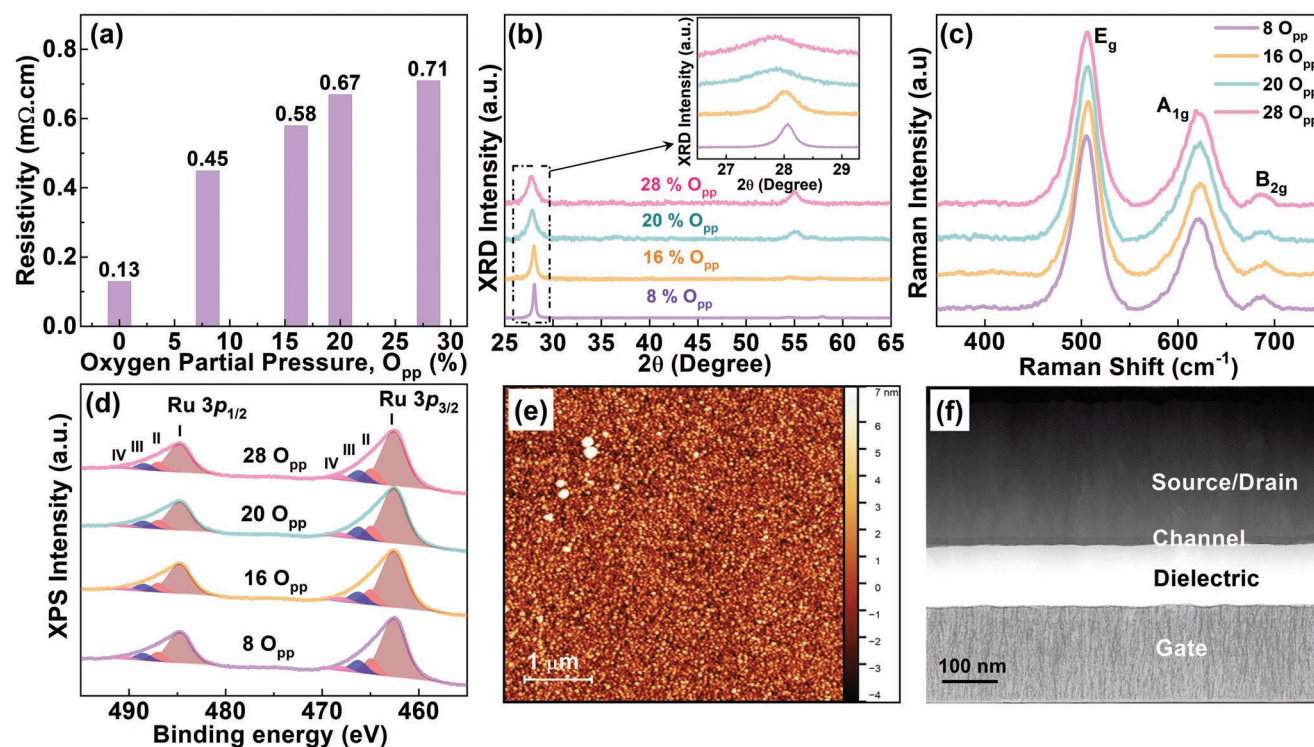


Figure 2. a) Variation of RuO_2 thin film resistivity deposited in different oxygen partial pressures. b) XRD diffraction patterns obtained from the same RuO_2 films deposited on glass substrate. The inset shows high-resolution XRD spectra for (110) plane. c,d) The comparison of Raman spectra (c) and XPS spectra (d) for different RuO_2 thin films. XPS curve fitting revealed the existence of multioxidation state of Ru and absorbed moisture in the oxide films. e) The atomic force microscopy (AFM) surface profile shows a smooth surface with a surface roughness value of 1.95 nm (RMS). f) The high-resolution cross-section transmission electron microscopy (TEM) image of a typical multilayer stack used to fabricate TFTs.

values are found to be comparable to previously reported resistivity values of sputtered RuO₂.^[17]

The crystallinity of RuO₂ thin films deposited on glass substrates was investigated using X-ray diffraction (XRD), as shown in Figure 2b. The major crystalline peak corresponding to (110) planes of RuO₂ is present at $2\theta = 28^\circ$ for all samples. It is noticeable that the peak becomes broad for RuO₂ films deposited at higher O_{pp}. Another broad peak was found at 55° corresponding to the (211) planes for the samples deposited using more than 20% O_{pp}. These peaks are consistent with the rutile crystal structure of RuO₂.^[18,19] The RuO₂ thin films are further characterized by Raman spectroscopy (Figure 2c), which shows three major Raman vibration modes, including E_g, A_{1g}, and B_{2g} located at ≈ 505 , 621, and 685 cm⁻¹, respectively. The E_g and A_{1g} peaks are found to be broad with a redshift at higher O_{pp}, indicating less ordered films.^[20,21] The XRD and Raman shifts obtained from pure Ru (0 O_{pp}) were also studied as a reference, and are shown in Figure S2b,c (Supporting Information), respectively.

The chemical compositions of different RuO₂ thin films were analyzed using X-ray photoelectron spectroscopy (XPS), as shown in Figure 2d. It can be observed that the XPS spectrum for Ru 3p is a doublet, with 3p_{3/2} and 3p_{1/2} observed at lower and higher binding energies, respectively. The thin films show no metallic Ru, rather they are fully oxidized and peak fitted to four components. The main intense peaks at 462.7 and 484.9 eV are attributed to Ru⁴⁺ (shown as region "I" in Figure 2d).^[22] The three small peaks at higher binding energy are attributed to absorbed moisture: RuO_x·yH₂O (at 464.8 and 486.9 eV (region "II")), Ru⁶⁺ of RuO₃ (at 466.3 and 488.6 eV (region "III")), and Ru⁸⁺ of RuO₄ (at 468.1 and 490.3 eV (region "IV")).^[23,24] It was noticed that the peaks shift slightly toward higher binding energies with increasing O_{pp} values. Also, from the XPS curve fitting results, it was found that the amount of RuO_x·yH₂O increases with increasing O_{pp}. For example, about 8% higher RuO_x·yH₂O was observed for RuO₂ films deposited at 28% O_{pp} as compared to 8% O_{pp} RuO₂ films. The surface morphology of the RuO₂ thin film deposited under 28% O_{pp} was inspected using atomic force microscopy and is shown in Figure 2e. The RMS value of roughness was found to be 1.95 nm for the 250 nm thin film on a glass substrate. Figure 2f shows a high-resolution cross-section dark field scanning transmission electron microscope image of a typical multilayer stack used to fabricate rectifiers in this study. All layers can be clearly identified with relatively sharp interfaces, which illustrates the uniform deposition process of the different layers.

TFTs were developed and used to fabricate on-chip rectifiers which were subsequently integrated with the electrochemical microsupercapacitors. Our goal was to make thin film transistors in the bottom gate configuration, wherein the transistor gate material (RuO₂) is the same material used for the electrochemical microsupercapacitors electrodes. A typical structure of our TFTs is shown in Figure S4 (Supporting Information). From our previous report,^[25] we know that ZnO (≈ 25 nm) as a channel layer and HfO₂ (≈ 130 nm) as a gate dielectric can give good TFT performance and hence we started our study considering these facts. Notice that the gate material is made with RuO₂, which is the first report on ZnO-based TFTs using RuO₂ as gate electrodes. The output and transfer curves obtained

from a typical TFT are shown in Figure 3a,b, respectively. It can be seen that the output curves show good saturation with no hysteresis in the transfer characteristic curves. The fabricated TFTs show high $I_{\text{on}}/I_{\text{off}}$ ratio of $>10^8$, a subthreshold swing of ≈ 791 mV dec⁻¹, and high saturation mobility (μ_{sat}) of ≈ 12.82 cm² V⁻¹ s⁻¹ with a turn-ON voltage of ≈ -2.13 V. The TFT performance obtained with RuO₂ as a gate electrode is comparable to ZnO-based TFTs reported in the literature.

Thin film transistor rectifiers (TFTRs) are designed and fabricated in this study by shorting the gate to drain terminals of the transistor; in this way, the device operates only in saturation region following the relationship: $V_{\text{in}} > V_{\text{Dsat}} + V_{\text{th}} > V_{\text{ON}}$. Hence, the gate to drain short terminal acts as an anode (input terminal) of the TFTR and the source terminal acts as a cathode (output terminal). Therefore, during the application of the positive bias to the anode, charge accumulation in the channel/gate dielectric occurs due to electric field effect and, as a result, the diode conducts resulting in forward bias configuration just like a conventional diode. The electrons are depleted from the channel/gate dielectric interface under the application of the negative voltage to the anode terminal. Hence, the TFTR becomes reversed biased which prevented negative voltages from passing through the diode. By shorting the gate to drain terminals of the TFTs mentioned above, we obtained a poor DC rectification ratio of $\approx 10^4$ times only (Figure 3c). It can be observed that the forward current of the TFTR at 10 V is comparable with the ON current of the TFT. However, the reverse biased current of the TFTR is on the order of $\approx 10^{-8}$, whereas the OFF current of the TFTs is on the order of $\approx 10^{-12}$. We believe that the negative turn-ON voltage of the TFTs limited it to be fully depleted resulting in high reversed bias leakage current. We took a strategy to reduce the reverse biased rectifier leakage current by shifting the turn-ON voltage to higher positive values while keeping the same electron mobility, and ON current. We shifted turn-ON voltage by reducing the thickness of the channel layer keeping other layers of the TFTs unchanged. However, beyond a certain thickness of the channel layer, the mobility and the ON current start reducing significantly. Here, we included TFT performance obtained from the devices with channel thicknesses of ≈ 20 nm and ≈ 14 nm. Good current saturation was obtained in both devices as shown in Figure 3d,g. Also, from the transfer curves, it was found that the turn-ON voltage reduces to 0.75 V for the TFT with a channel thickness of ≈ 14 nm (see Figure 3h). However, the saturation mobility was slightly reduced (≈ 11.96 cm² V⁻¹ s⁻¹), but still acceptable for the rectification operation. Also, an ON/OFF ratio of $\approx 10^9$ and low SS of 417 mV dec⁻¹ were obtained. A good DC rectification ratio of $\approx 10^7$ times at ± 10 V was obtained (Figure 3i). This rectification ratio is comparable to many p-n junctions, and Schottky diodes reported elsewhere.^[26–28]

For the AC performance of a single stage TFTR, the output signal was captured using an oscilloscope across a load resistance (Figure 4a). Figure 4b shows applied input sinusoidal signals (1 kHz frequency) with different peak to peak voltage values. The output half wave signals obtained using different external loads including 5.5k, 10k, 46k, 67k, 98k, 110k, and 10 M Ω are shown in Figure 4c. It was found that with increasing load resistance, the positive maximum peak voltage increases up to 4.48 V when 110 k Ω resistance was used as an

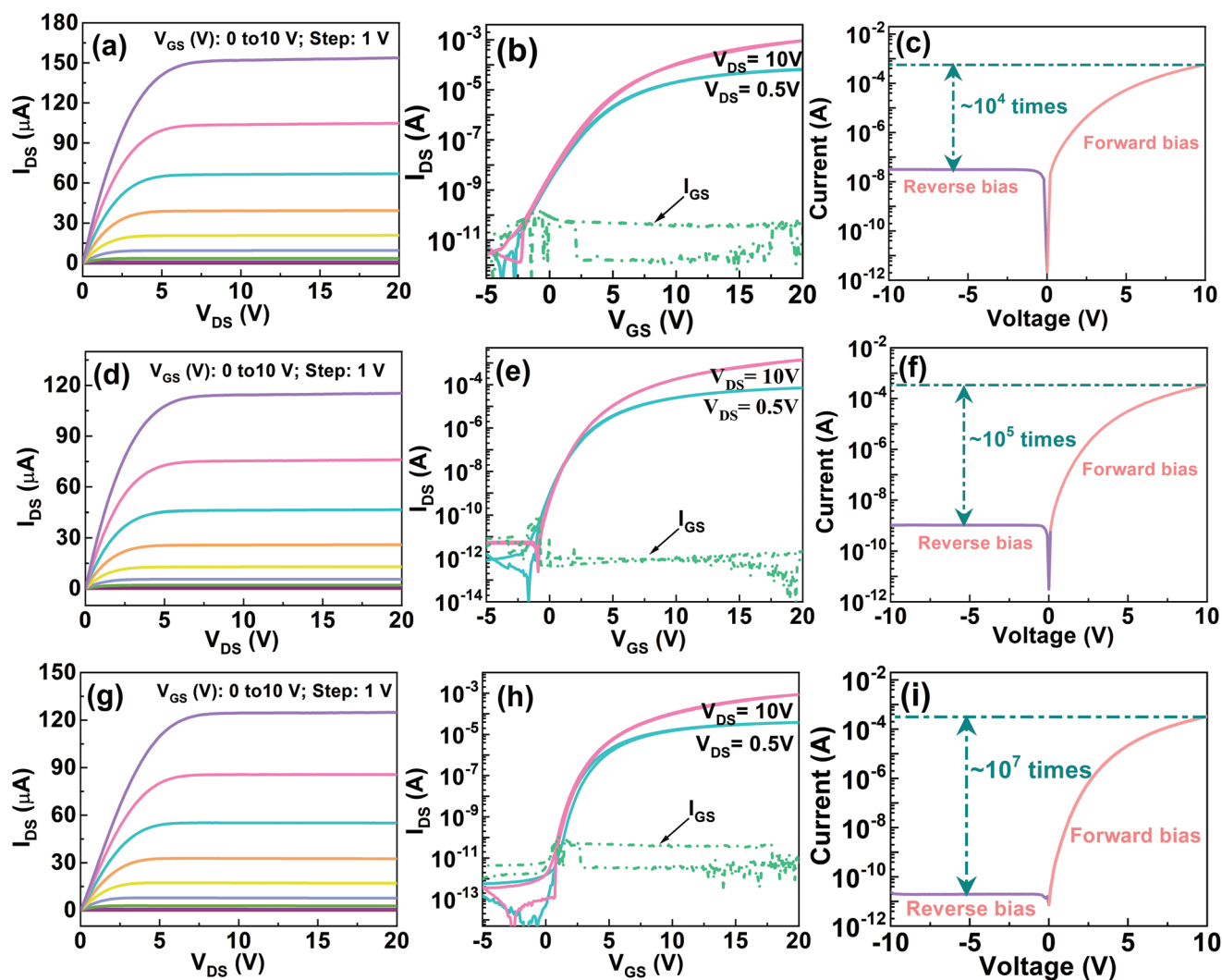


Figure 3. Optimization of the thin film transistor and rectifier performance with RuO_2 gate contacts. a–c) The output (a), transfer (b), and DC rectification (c) performance obtained from devices using 25 nm ZnO channel thickness. d–f) The output (d), transfer (e), and DC rectification (f) performance obtained from devices using 20 nm ZnO channel thickness. g–i) The output (g), transfer (h), and DC rectification (i) performance obtained from devices using 14 nm ZnO channel thickness. A DC rectification ratio of $\approx 10^7$ was achieved using 14 nm channel thickness. The RuO_2 gate electrode thickness was maintained at 250 nm.

external load. However, the peak voltage decreases to 800 mV with the use of 10 M Ω as an external load. In our remaining study, we used 110 k Ω as the external load.

However, it was found that the output signals contain a smaller voltage amplitude as compared to the input signals (Figure 4d), which implies some voltage drop across the TFTR (as the channel has a finite resistance).^[29] With fixing external load (110 k Ω) and peak to peak voltage of 20 V, different input signals with varying frequency were studied to monitor output performance, as shown in Figure 4e. It was found that the TFTR performed well in the frequency range of 10 Hz to 30 kHz. At frequencies higher than 30 kHz, the output signal did not follow the input signal well, resulting in poor rectification. Even though the higher cut-off frequency of our TFTRs is smaller than conventional diodes, it is still suitable for many self-powered sensors, where a signal with a frequency range from few Hz to several kHz is required. In context, the TFTR

with -2.13 V as turn-ON voltage shows AC rectification up to 200 Hz only (see Figure S6, Supporting Information).

Also, the TFTRs were characterized with the output signal of a homemade triboelectric nanogenerator (TENG). A typical TENG signal which was used as an input signal to the TFTR, and the half-wave rectified signal is shown in Figure S7 (Supporting Information). This result shows that our TFTRs with RuO_2 electrodes can be used to rectify different input AC signals, including those generated by TENGs.

For self-powered systems, microsupercapacitors offer several advantages as integrated micropower sources. We fabricated microsupercapacitors with interdigital electrodes using the same RuO_2 material used for transistor and rectifier contacts to facilitate their on-chip integration. RuO_2 thin films containing higher $\text{RuO}_x \cdot \gamma \text{H}_2\text{O}$ content were used to improve supercapacitor performance.^[30] The electrochemical performance was evaluated using a polymer gel electrolyte poly(vinyl alcohol)

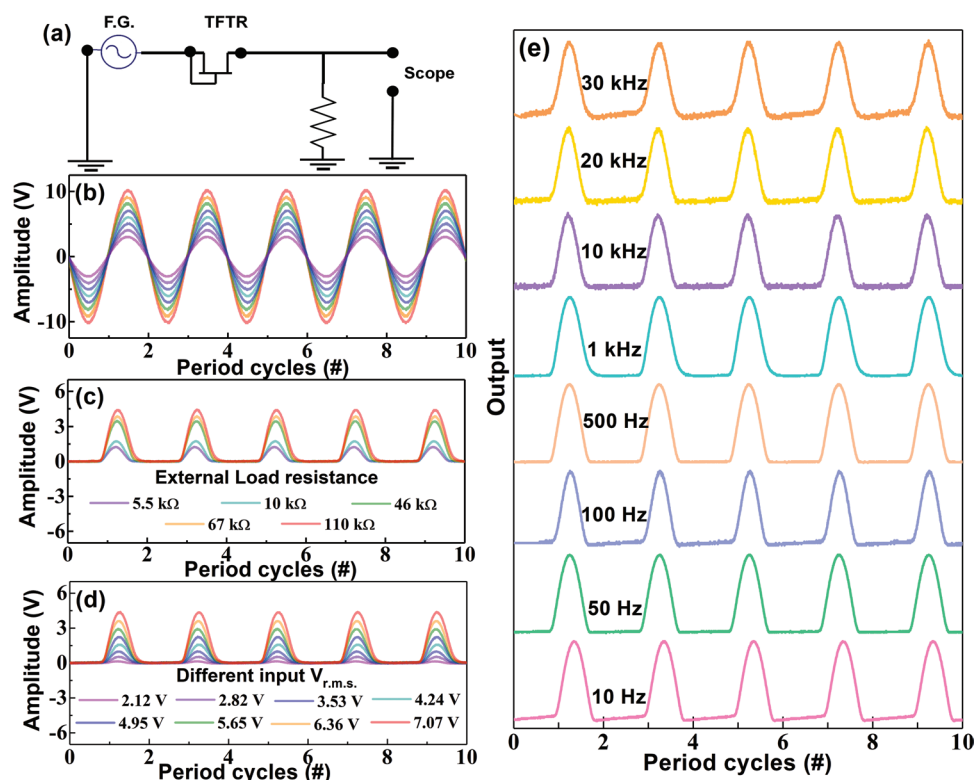


Figure 4. a) Circuit diagram of the set-up used to measure AC rectification of RuO₂-gated thin film transistor rectifiers. b) Sinusoidal AC input signals with different amplitudes. c) Half wave output signals obtained across different external loads. d) Half wave output signals obtained after the application of different peak to peak voltage-based input signals. e) Half wave output signals obtained under the application of different input signals carrying different frequency.

(PVA)–H₂SO₄) cross-linked with glutaraldehyde (GA). Four gel electrolyte solutions prepared using 0.5, 2.5, 5, and 10 mass% GA, respectively, were added into PVA–H₂SO₄ solution. The cyclic voltammetry (CV) measurements were performed using these four-gel electrolytes coated on identical RuO₂ micro-supercapacitors, as shown in Figure 5a. It can be seen that nearly rectangular CV curves with a potential window of 1.0 V were obtained for all devices under a scan rate of 100 mV s^{−1}. The absence of oxidation and reduction peaks with near rectangular CV shape shows nearly ideal capacitive behavior with excellent reversibility, high rate capability, fast redox reactions at the surfaces of the electrodes. Further, it was found that the area under the CV curve increases with decreasing GA amount. This means that a critical volume of the cross-linking agent is required to achieve good performance, where the gel electrolyte can produce sufficient ions and good quality interface between active electrodes/electrolyte.^[31,32] The solidification of the gels increases dramatically with increasing GA content leading to higher internal resistance. As a result, the electrochemical performance degrades at higher volumes of GA.^[33]

The capacitive behavior was further investigated using galvanostatic charge–discharge (CD) measurements at a fixed current density of 0.1 mA cm^{−2}, as shown in Figure 5b. All CD curves show near linear and symmetric charge and discharge profiles, which suggests an excellent capacitive behavior with a rapid current–voltage response. The highest capacitance values were obtained for the MSC with 0.5% GA (Figure 5c).

It should be noted that the areal capacitance values in our RuO₂-based MSCs are small as compared to chemically derived RuO₂ electrode (e.g., Liu et al. reported areal capacitance of 40.7 mF cm^{−2}^[34]) or even conventional carbon-based MSCs (e.g., Kou et al. reported areal capacitance of 177 mF cm^{−2} in reduced graphene oxide (rGO)/carbon nanotube (CNT)-based supercapacitors^[35]). The small capacitance is mainly due to three reasons: 1) lack of sufficient water in the sputtered RuO₂ thin films, as compared to chemically derived RuO₂, which limits protonic conduction in the bulk of the active material;^[36] 2) sputtered RuO₂ electrode surface is very smooth, and has almost no pores, which reduces the electrochemically active surface area of the electrodes; 3) thickness of the RuO₂ electrodes is only ≈250 nm, which is significantly smaller than thickness of electrodes used in conventional MSCs.^[37–40] However, the volumetric capacitance of our microsupercapacitors is still comparable to many reported carbon-based microsupercapacitors. A comparison of the areal and volumetric capacitance of our RuO₂ with several other materials is presented in Table S1 in the Supporting Information section.

The effect of RuO₂ electrode thickness on electrochemical properties was also investigated with four different RuO₂ thicknesses (125, 250, 500, and 750 nm). The CV and CD curves are presented in Figure 5d,e, respectively. It can be seen that the areal capacitance increases with RuO₂ thickness, as shown in Figure 5f, which can be attributed to the increased electrode surface area exposed to the electrolyte. Further details

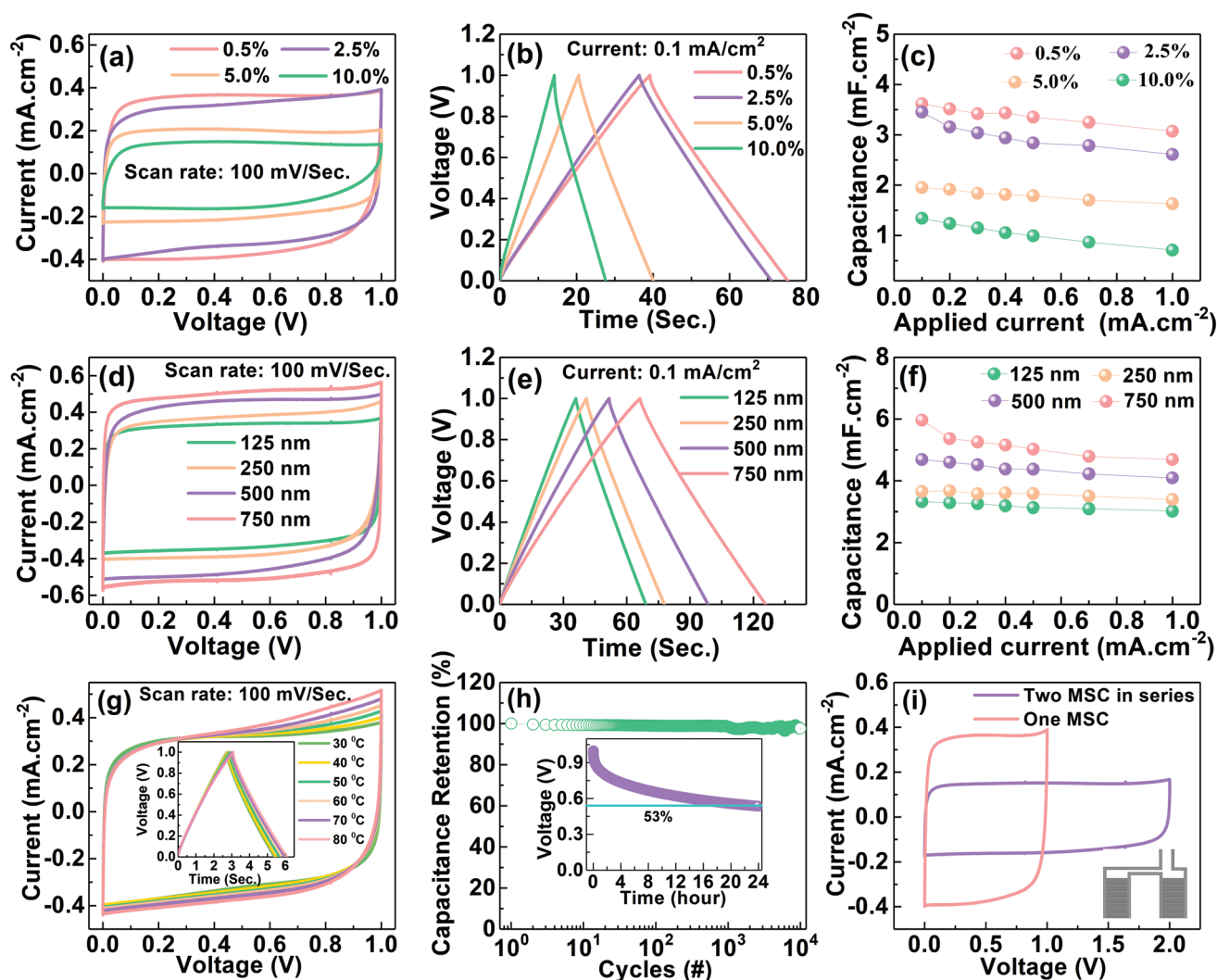


Figure 5. Performance of microsupercapacitors sharing same RuO₂ electrodes with thin film rectifiers. a) CV, b) CD, and c) effect of glutaraldehyde amount in electrolyte on areal capacitance. d) CV, e) CD, and f) effect of RuO₂ electrode thickness on areal capacitance. g) The CVs and CDs obtained from 250 nm RuO₂ MSCs at different temperatures. h) Cycling test is showing $\approx 95\%$ capacitance after 10 000 continuous cycles. The inset shows that excellent self-discharge characteristics (18.75 mV h^{-1}) can be achieved using our RuO₂ electrodes. i) CV curve obtained from two identical MSCs connected in series.

on the CV and CD curves of MSCs obtained from different gel electrolyte, and RuO₂ thicknesses are shown in Figures S8 and S10 (Supporting Information), respectively. For the remaining works, we selected 250 nm thick RuO₂ electrodes because they offer a compromise between MSC performance and ease of TFTR fabrication.

In practical operation, electronic circuits generate heat. Thus the temperature dependence CV and CD (inset) curves were also studied in the range of 30–80 °C (Figure 5g), which show a stable electrochemical performance even at a higher temperature, signifying that our devices remain stable during high-temperature operation. A small improvement in both CVs and CDs was noticed with increasing temperature, which is possibly due to improved ionic conductivity at the higher temperature. On the other hand, nearly 95% of the initial capacitance was retained after 10 000 continuous charge/discharge cycles (Figure 5h).

Another critical aspect of microsupercapacitors performance for self-powered applications is the self-discharge rate of MSCs,

which was studied by charging an MSC device to 1 V for 40 s, and then monitoring the self-discharge process as shown in the inset of Figure 5h. It was found that our MSCs can hold 55% of initial voltage even after 24 h, with a slow decay rate of $\approx 18.75 \text{ mV h}^{-1}$, which is sufficient for many miniature devices that intermittently measure and transmit signals, where they literally need the power for 10–20 s. The power output characteristics were studied using Ragone plot, as shown in Figure S11b (Supporting Information). It can be seen that the energy density decreases with increasing power density. A maximum energy density of $19.21 \text{ mWh cm}^{-3}$ was achieved at a power density of 2 W cm^{-3} . In modern implantable and wearable electronic devices, a power supply in the range of 1–100 μW is required.^[41,42] As an example, for modern pacemakers, the required maximum power is only 1 μW .^[43,44] Therefore, the energy consumption for such devices with 1 μW power for 1 h is about 3600 μJ , which corresponds to a capacitance of $\approx 7.2 \text{ mF}$. However, micropower sources especially for sensing

applications are mostly in standby mode, and are only active for seconds to collect data. Thus, the power density of our microsupercapacitors is sufficient to power such devices on an intermittent basis. On the other hand, while a potential window of 1 V was obtained with one MSC, it can be increased to 2 V by connecting two MSCs in series (Figure 5i).

The on-chip storage performance of the integrated micro-supercapacitor–thin film rectifier system is first demonstrated by charging one single MSC using the AC signal from a function generator. The circuit arrangement for this study is shown in Figure S12 (Supporting Information). Before applying any signal to the MSC, the two electrodes were shorted to remove any pre-stored charges (Figure 6a, region “I”). Sinusoidal AC signals with different frequencies (a constant peak-to-peak voltage of 20 V) were applied to the input terminal of the TFTR, and the output of the TFTR was applied directly to MSC to charge

it up to 1 V (Figure 6a, region “II”). After reaching to 1 V, the input signal was shut down, and the stored charge in the form of voltage was monitored for 100 s (Figure 6a, region “III”) before shorting the two MSC electrodes again (Figure 6a, region “IV”). It was found that the MSC charging rate is $\approx 34 \text{ mV s}^{-1}$, which decreases with increasing frequency of the applied input signals (Figure 6b). On the other hand, the effect of peak-to-peak voltage of the input signal on MSC charging was also monitored as shown in Figure 6c. Different input signals were allowed to charge the MSC through the TFTR for 40 s and then the input signal was cut off. It was found that the charging rate increases with increasing peak to peak voltage of the applied input signals, as shown in Figure 6d. However, it was found that no charging occurs with the application of the input signal of 5 V peak to peak voltage, which is not sufficient to charge the MSCs during the allotted time. The optical image of a real

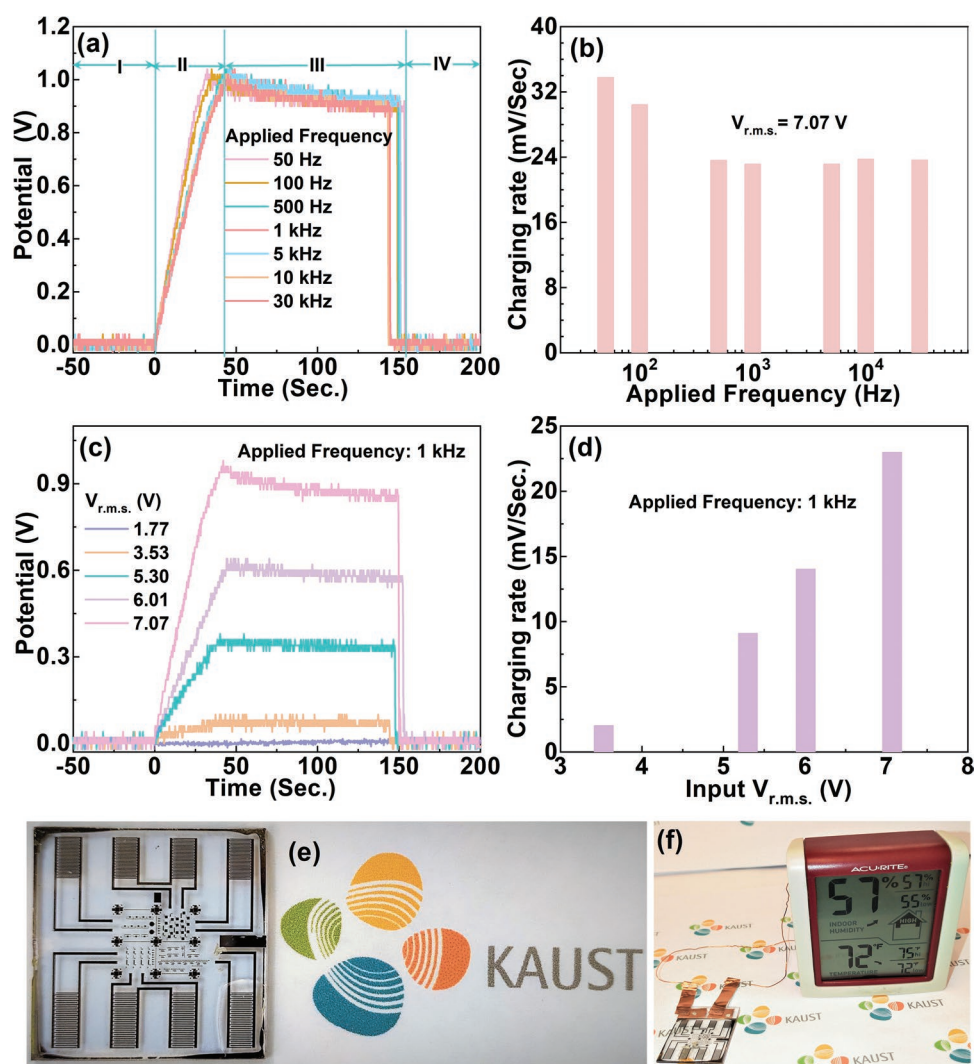


Figure 6. Integrated microsupercapacitors–thin film rectifier unit demonstration. Different sinusoidal signals were obtained from a function generator (to simulated harvested energy), stored, and then discharged to power actual device. a) Charging of MSC using A.C. signals carrying different frequencies. b) Variation of charging rate at different input frequencies. c) Charging of MSC using different peak to peak voltage amplitude input signals. d) Variation of the charging rate at different RMS values of the input signals. e) Optical image of the actual integrated device, with the KAUST logo. f) Powering off a commercial hygro-thermograph device by the chip shown in (e).

on-chip device is shown in Figure 6e, next to the KAUST logo. Also, we demonstrated in Figure 6f that our microsupercapacitors can power up a commercial digital hygro-thermometer.

In summary, we have demonstrated the integration of electrochemical microsupercapacitors and thin film electronics using a single contact material (RuO_2) for both devices. Our thin film rectifiers can replace bulky packaged Si rectifiers that have been typically used in self-powered sensor systems. This can lead to truly on-chip energy storage at the transistor level, which could revolutionize the self-powered sensor by making them more compact and more compatible with standard fabrication methods. In fact, our common electrode material concept can in principle be realized using other electrochemically active materials such as graphene, MXene, and other oxides. The functionality of the integrated electrochemical microsupercapacitors–thin film rectifier system was also successfully demonstrated using triboelectric nanogenerator and AC input signals, which was properly stored, and used to power several electronic devices.

Experimental Section

Experimental details including material deposition, device fabrication, and characterizations can be found in the Supporting Information.

Supporting Information

Supporting Information is available from the Wiley Online Library or from the author.

Acknowledgements

Research reported in this publication was supported by King Abdullah University of Science and Technology (KAUST) under the Sensors Initiative (grant number CRF-2015-SENSORS-2709). The authors thank the core laboratory and the imaging and characterization staff at KAUST for their support.

Conflict of Interest

The authors declare no conflict of interest.

Keywords

microsupercapacitors, on-chip energy storage, RuO_2 , thin film rectifiers, thin film transistors

Received: November 18, 2018
Revised: April 11, 2019
Published online: May 6, 2019

- [1] I. R. Mineev, P. Musienko, A. Hirsch, Q. Barraud, N. Wenger, E. M. Moraud, J. Gandar, M. Capogrosso, T. Milekovic, L. Asboth, R. F. Torres, N. Vachicouras, Q. Liu, N. Pavlova, S. Duis, A. Larmagnac, J. Vörös, S. Micera, Z. Suo, G. Courtine, S. P. Lacour, *Science* **2015**, *347*, 159.

- [2] B. C.-K. Tee, C. Wang, R. Allen, Z. Bao, *Nat. Nanotechnol.* **2012**, *7*, 825.
[3] C. R. Merritt, H. T. Nagle, E. Grant, *IEEE Sens. J.* **2009**, *9*, 71.
[4] P.-K. Yang, L. Lin, F. Yi, X. Li, K. C. Pradel, Y. Zi, C.-I. Wu, J.-H. He, Y. Zhang, Z. L. Wang, *Adv. Mater.* **2015**, *27*, 3817.
[5] B. Wang, M. Ahmed, B. Wood, F. Iacopi, *Appl. Phys. Lett.* **2016**, *108*, 183903.
[6] J. Li, V. Mishukova, M. Ostling, *Appl. Phys. Lett.* **2016**, *109*, 123901.
[7] N. Liu, Y. Gao, *Small* **2017**, *13*, 1701989.
[8] Y. Da, J. Liu, L. Zhou, X. Zhu, X. Chen, L. Fu, *Adv. Mater.* **2018**, *31*, 1802793.
[9] D. P. Dubal, N. R. Chodankar, D. H. Kim, P. G. Romero, *Chem. Soc. Rev.* **2018**, *47*, 2065.
[10] P. Zhang, F. Wang, M. Yu, X. Zhuang, X. Feng, *Chem. Soc. Rev.* **2018**, *47*, 7426.
[11] N. A. Kyeremateng, T. Brousse, D. Pech, *Nat. Nanotechnol.* **2017**, *12*, 7.
[12] H. Hun, Z. Pei, C. Ye, *Energy Storage Mater.* **2015**, *1*, 82.
[13] Q. Jiang, C. Wu, Z. Wang, A. C. Wang, J.-H. He, Z. L. Wang, H. N. Alshareef, *Nano Energy* **2018**, *45*, 266.
[14] X. Pu, M. Liu, L. Li, C. Zhang, Y. Pang, C. Jiang, L. Shao, W. Hu, Z. L. Wang, *Adv. Sci.* **2016**, *3*, 1500255.
[15] K. Dong, J. Deng, Y. Zi, Y. C. Wang, C. Xu, H. Zou, W. Ding, Y. Dai, B. Gu, B. Sun, Z. L. Wang, *Adv. Mater.* **2017**, *29*, 1702648.
[16] Y. M. Lu, W. S. Hwang, W. Y. Liu, J. S. Yang, *Mater. Chem. Phys.* **2001**, *72*, 269.
[17] D. Buc, M. Mikula, D. Music, U. Helmersson, P. Jin, S. Nakao, K. Y. Li, P. W. Shum, Z. Zhou, M. Caplovicova, *J. Electr. Eng.* **2004**, *55*, 39.
[18] J. W. Long, K. E. Swider, C. I. Merzbacher, D. R. Rolison, *Langmuir* **1999**, *15*, 780.
[19] B. Y.-L. Chueh, C.-H. Hsieh, M.-T. Chang, L.-J. Chou, C. S. Lao, J. H. Song, J.-Y. Gan, Z. L. Wang, *Adv. Mater.* **2007**, *19*, 143.
[20] S. Bhaskar, P. S. Dobal, S. B. Majumder, R. S. Katiyar, *J. Appl. Phys.* **2001**, *89*, 2987.
[21] G. J. Exarhos, N. J. Hess, *Thin Solid Films* **1992**, *220*, 254.
[22] V. Kruefu, A. Wisitsoraat, D. Phokharatkul, A. Tuantranont, S. Phanichphant, *Sens. Actuators, B* **2016**, *236*, 466.
[23] W. Wang, S. Guo, I. Lee, K. Ahmed, J. Zhong, Z. Favors, F. Zaera, M. Ozkan, C. S. Ozkan, *Sci. Rep.* **2015**, *4*, 4452.
[24] C. Mun, J. J. Ehrhardt, J. Lambert, C. Madic, *Appl. Surf. Sci.* **2007**, *253*, 7613.
[25] P. K. Nayak, Z. Wang, D. H. Anjum, M. N. Hedhili, H. N. Alshareef, *Appl. Phys. Lett.* **2015**, *106*, 103505.
[26] S. Narushima, H. Mizoguchi, K. Shimizu, K. Ueda, H. Ohta, M. Hirano, T. Kamiya, H. Hosono, *Adv. Mater.* **2003**, *15*, 1409.
[27] A. Chasin, M. Nag, A. Bhoolokam, K. Myny, S. Steudel, S. Schols, J. Genoe, G. Gielen, P. Heremans, *IEEE Trans. Electron Devices* **2013**, *60*, 3407.
[28] Y. C. Shin, J. Song, K. M. Kim, B. J. Choi, S. Choi, H. J. Lee, G. H. Kim, T. Eom, C. S. Hwang, *Appl. Phys. Lett.* **2008**, *92*, 162904.
[29] Y. Zhang, Z. Mei, S. Cui, H. Liang, Y. Liu, X. Du, *Adv. Electron. Mater.* **2016**, *2*, 1500486.
[30] M. K. Hota, Q. Jiang, Y. Mashraei, K. N. Salama, H. N. Alshareef, *Adv. Electron. Mater.* **2017**, *3*, 1700185.
[31] N. A. Choudhury, A. K. Shukla, S. Sampath, S. Pitchumani, *J. Electrochem. Soc.* **2006**, *153*, A614.
[32] W. G. Moon, G.-P. Kim, M. Lee, H. D. Song, J. Yi, *ACS Appl. Mater. Interfaces* **2015**, *7*, 3503.
[33] K.-J. Kim, S.-B. Lee, N.-W. Han, *Korean J. Chem. Eng.* **1994**, *11*, 41.
[34] C.-C. Liu, D.-S. Tsai, D. Susanti, W.-C. Yeh, Y.-S. Huang, F.-J. Liu, *Electrochim. Acta* **2010**, *55*, 5768.
[35] L. Kou, T. Huang, B. Zheng, Y. Han, X. Zhao, K. Gopalsamy, H. Sun, C. Gao, *Nat. Commun.* **2014**, *5*, 3754.

- [36] W. Sugimoto, H. Iwata, K. Yokoshima, Y. Murakami, Y. Takasu, *J. Phys. Chem. B* **2005**, 109, 7330.
- [37] P. Huang, C. Lethien, S. Pinaud, K. Brousse, R. Laloo, V. Turq, M. Respaud, A. Demortière, B. Daffos, P. L. Taberna, B. Chaudret, Y. Gogotsi, P. Simon, *Science* **2016**, 351, 691.
- [38] J. Lin, Z. Peng, Y. Liu, F. R. Zepeda, R. Ye, E. L. G. Samuel, M. J. Yacaman, B. I. Yakobson, J. M. Tour, *Nat. Commun.* **2014**, 5, 5714.
- [39] Z. S. Wu, K. Parvez, S. Li, S. Yang, Z. Liu, S. Liu, X. Feng, K. Müllen, *Adv. Mater.* **2015**, 27, 4054.
- [40] M. F. El-Kady, R. B. Kaner, *Nat. Commun.* **2013**, 4, 1475.
- [41] Z. L. Wang, *Nano Today* **2010**, 5, 512.
- [42] Z. L. Wang, W. Wu, *Angew. Chem., Int. Ed.* **2012**, 51, 11700.
- [43] M. A. Karami, D. J. Inman, *Appl. Phys. Lett.* **2012**, 100, 042901.
- [44] M. Beidaghi, Y. Gogotsi, *Energy Environ. Sci.* **2014**, 7, 867.